Turbulent Mixing in a Tubular Reactor: Assessment of an FDF/LES Approach

E. van Vliet, J. J. Derksen and H. E. A. van den Akker
Kramers Laboratorium voor Fysische Technologie, Faculty of Applied Sciences, Delft University of Technology, Prins Bernhardlaan 6, 2628 BW Delft, Netherlands

DOI 10.1002/aic.10365
Published online in Wiley InterScience (www.interscience.wiley.com).

The aim of the present research was to investigate the feasibility of a probability density function (PDF) methodology combined with a large eddy simulation (LES) for turbulent reactive mixing in industrial geometries. In order to incorporate the PDF transport equation into a LES context, a filtered version was employed, denoted as filtered density function (FDF) equation. Using FDF/LES, the yield of mixing-sensitive, parallel competitive reactants was numerically studied in a tubular reactor with perpendicular inlet operated at Re = 4,000 for varying Damköhler numbers and feed-stream concentrations. The "interaction by exchange with the mean" (IEM) model was used to close the filtered conditional scalar energy dissipation rate (SED) appearing in the FDF equation. The modeling assumptions were assessed by means of laser induced fluorescence (LIF) experimental data, providing the mean conserved concentration field in a horizontal and vertical center plane downstream the injector, and concentration PDF's at several downstream positions. In the vicinity of the injector, the FDF/LES model slightly overpredicts both the spreading of jet and the dissipation of small scale fluctuations, which was attributed to the overprediction of the turbulent diffusivity in the transition region of the laminar jet to the the turbulent wake of the injector. Further downstream, however, the global macro transport of the reactants was qualitatively well predicted, and the sensitivity of the yield to the Damköhler number and feedstream concentration showed consistent behavior. © 2005 American Institute of Chemical Engineers *AIChE J,* 51: 725–739, 2005

Keywords: FDF/LES, 3D-LIF, mixing, turbulence

Introduction

Mixing reacting scalars in turbulent flows is a crucial step in a wide range of industrial processes. Commonly, multiple, parallel reactions compete for a limited supply of reactants. In order to optimize the process conditions such that the formation of unwanted side products is minimized, an adequate description of the mixing process is needed.

A complete description of the reacting scalars without any modeling can be obtained by means of a direct numerical simulation (DNS); the transport equations of the fluid momentum and scalar components are solved on a numerical grid that captures the whole range of turbulent scales from the size of the reactor down to the smallest turbulent fluid and scalar scales, the Kolmogorov and Batchelor length scales [for example,[1]]. Since the flow in most industrial applications is highly turbulent, the range of length and time scales usually is very wide. Consequently, under these circumstances, this DNS approach is not quite feasible, and some way of modeling is required.

A rough categorization of modeling approaches can be made on the basis of the proportion of the fluid and scalar spectrum that is solved explicitly, and the proportion which is modeled. The classical treatment of turbulent flows is based on decomposing the dependent variables into mean and fluctuating com-

Correspondence for this article should be addressed to E. Van Vliet at eelco@klft.tn.tudelft.nl.

ponents (Reynolds decomposition). Models are required to close the cross-correlation terms that appear upon averaging the decomposed transport equations. Consequently, such RANS-models should cover the whole spectrum of turbulent scales. Since no distinction is made between the large and small scales, the models have to capture two distinctly different physical processes; turbulent convection at the large scales, and molecular diffusion at the small scales.

Mechanistic micromixing models rely on the idea that molecular diffusion and the resulting chemical reactions take place at the smallest turbulent scales; therefore, the advection-diffusion-reaction equation for a scalar within an assumed laminar flow field representing lamina in a single Kolmogorov eddy is solved explicitly [for example,[2–4]]. As a consequence, a separation of scales is incorporated into the mechanistic micromixing model; the high end of the scalar spectrum is solved explicitly, and the cascade from the large down to the small scales is modeled. Usually, computational nodes that represent the locations of the reaction zones are tracked within the flow field calculated separately according to, for example, a RANS-approach. Dedicated models are adopted to capture the turbulent cascade of the reaction zone in order to predict its current length scale. The micromixing advection-diffusion starts at the moment the Kolmogorov length scale (or some other scale related) is reached. Since the result of the approach depends on the way the complicated and nonuniversal cascade process is modeled, one could wonder whether it is useful to put all computational power into the numerical solution of the scalar advection-diffusion at scales that are predicted so crudely. Moreover, at the moment of release of the computational nodes, it is not known *a priori* what the Kolmogorov eddy size will be, since it depends on the turbulent region where it will arrive in the reactor. Since the initial properties of a computational node depend on their unknown future state, micromixing models are non-causal, and, consequently, it is in principle not possible to set the initial conditions (such as the amount of reactant dye fed to the reactor).

With a large eddy simulation (LES) approach, a low-pass filter is applied to the transport equations of the fluid and the large-scale motions of the fluid are solved explicitly. Modeling applies to the nonresolved high-frequency part of the turbulent spectrum only. With the assumption that the small-scale fluctuations are in local equilibrium, some amount of universal behavior may be expected. In this work, a conventional[5] subgrid scale (SGS) model with a low mesh Reynolds number correction[6] has been employed in order to prevent overprediction of the eddy viscosity in the regions where the smallest turbulent scales are practically resolved. The LES approach has proven to be an important engineering tool to solve the turbulent flow in numerous industrial applications, such as stirred tanks (for example,[7,8]) or full scale crystallizers[9]).

In order to couple reactive scalar transport to the fluid flow LES, the transport equation of the scalar joint probability density function (PDF) is solved (for example,[10]). The primary advantage is that the reaction rate terms within these equations remain closed, and, thus, do not need any modeling. In order to incorporate PDF methods in LES, several methods have been proposed. In the field of combustion, for example, the conditional source-term estimation method (for example,[11]), and the presumed beta-function PDF method (for example,[12]) are used. In this work, the "filtered density function" (FDF) is employed[13] which in fact is the PDF of the SGS scalar components: Pope[13] demonstrated on formal mathematical grounds that the reaction rate appears in closed form in the FDF transport. Gao and O'Brien[14] developed a transport equation for the FDF, and offer suggestions for the remaining unclosed terms in this equation. Colucci et al.[15] and Zhou and Pereria[16] applied the FDF methodology to a temporally developing mixing layer and a spatially developing planar jet under both nonreacting and reacting (single reaction) conditions, and showed close agreement with DNS results. Variable density was included by Jaberi et al.[17] Van Vlict et al.[18] extended the FDF method to parallel, competitive reactions of the type $\mathcal{A} + \mathcal{B} \rightarrow \mathcal{P}$ and $\mathcal{A} + \mathcal{C} \rightarrow \mathcal{Q}$ (with a reaction rate $\overset{k_1}{\rightarrow}\overset{k_2}{\rightarrow}$), and demonstrated that the dependency of the yield on the Damköhler number (Da) was correctly predicted. Nowadays, FDF/LES is used for more complex reactions schemes (for example,[19]), or velocity fluctuations (for example,[20,21]).

The N_s dimensional FDF transport equation (N_s being the number of scalar components) is most naturally solved within a Lagrangian Monte Carlo (MC) framework. Computational particles representing the scalar composition evolve in both the compositional and spatial domain according to stochastic differential equations, such that the statistics of the particle ensemble corresponds to the modeled FDF equation. In this way, the computational effort depends only linearly rather than exponentially on the number of scalar species involved; this results in a major reduction in computational time. Unfortunately, the statistical accuracy increases with the square root of the number of MC particles only. For this reason, until so far the FDF method was only tested and applied to simple flows on relatively small computational grids in order to keep the computational time and memory requirements acceptable.

The aim of this article, is (1) to demonstrate that, given the current state of computational resources, the FDF method can be applied to an LES of reactive mixing in an industrially applied tubular reactor (TR), and (2) to validate the FDF model by means of experimental data. For the former purpose, a parallel cluster of eleven Linux PCs was employed, each equipped with a dual Athlon (TR) 1800+ processor, and one Gb of memory. As mentioned earlier, the reaction terms remain closed within the FDF context, and modeling applies to the conditional scalar energy dissipation rate (SED), and the subgrid scalar flux; hence, for the second purpose, it is relevant to assess the mixing of a conserved scalar while discarding chemical reactions. We use the experimental data of LIF measurements of the 2-D concentration field downstream the injector[22] in a horizontal and vertical center plane.

In the next section, the geometry of the TR is introduced, and the most relevant turbulent and kinetic length and time scales are estimated. Then, the numerical aspects are treated; the transport equations are given, and the SGS model employed to capture micromixing in the FDF context is introduced and discussed. Furthermore, the practical aspects of the simulations are presented. Next, the main results are presented in two parts: in the first part, only conserved scalar mixing is considered and compared to the LIF experimental data, whereas the second part focuses on the reactive scalar mixing for varying Damköhler numbers and inlet concentrations.

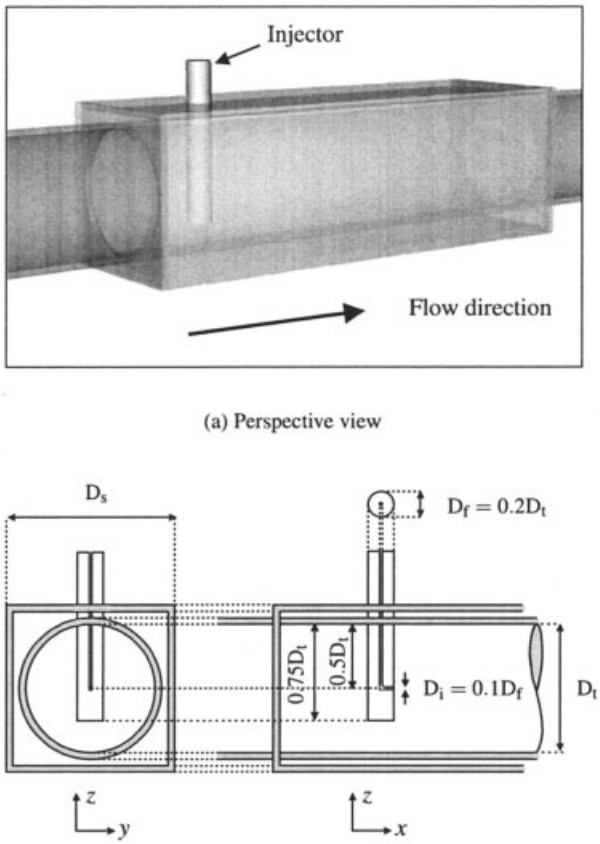

Figure 1. Perspective (a) and representation (b) of the tubular reactor at the position of the injector.

The definition of the coordinate system is given below Figure 1b. The square box is installed for experimental purposes only (see[22]).

Turbulent Reacting Flow Definition

A view of the TR is given in Figure 1. The reactor consists of a round tube (diameter D_t) in which a turbulent fluid flow is established containing some of the dissolved reactants. Other reaction components are added to the flow system via a feed pipe (dia. $D_f = 0.2D_t$) that protrudes into the main stream. It produces a jet pointing in the same direction as the main flow through a nozzle (dia. $D_i = 0.1D_f$) located at the downstream side of the feed pipe, at the centerline of the main tube.

The turbulent flow in the TR is characterized by several Reynolds numbers that are related to distinct sources of turbulence production. First, the mean flow through the reactor establishes a wall bounded shear flow. A Reynolds number based on the mean bulk velocity U_m is defined as $Re_m = U_m D_t/v$ (where, v is the kinematic viscosity of the fluid). Second, a turbulent wake is formed downstream of the injector that is characterized by the Reynolds number, based on the feed pipe dia. $Re_f = U_m D_f/v$, and the Strouhal number $St = D_f/(U_m \mathcal{T}_v)$. Here, the time scale $\mathcal{T}_v$ is the period between shedded vortices. Finally, the jet induces a free shear flow that is characterized by the jet Reynolds number $Re_i = U_f D_i/v$ (where, U_f the initial jet velocity), and the velocity ratio U_f/U_m.

The flow geometry and conditions were chosen to carefully represent the experimental flow facility of.[22] Since, in the experiment, the mean bulk velocity was limited for reasons of temporal resolution, measurements were performed at a moderate Reynolds number of $Re_m = 4{,}000$. The Reynolds numbers Re_f and Re_i both were 800. In this regime, vortex shedding occurs in the "irregular" regime, with a Strouhal number of about 0.2.[23] Since $D_t/D_f = 5$, the shedding time scale happens to be approximately equal to the macro time scale $\mathcal{T} = D_t/U_m$.

The main flow entering the inlet cross-section of the TR consisted of a homogeneous solution of reactants $\mathcal{B}$ and $\mathcal{C}$ with equal concentrations $\phi_{\mathcal{B}_0} = \phi_{\mathcal{C}_0} = 1$ (concentrations are denoted in arbitrary units). Reactant $\mathcal{A}$ was dissolved in the stream injected by the feed pipe with either a high or a low inlet concentration of $\phi_{\mathcal{A}_0} = 4{,}000$ or $\phi_{\mathcal{A}_0} = 1$, respectively. With the high inlet concentration case (denoted as H in table 1), an equal initial mass flux through the reactor for all reactants was established such that reactant $\mathcal{A}$ can either completely react with reactant $\mathcal{B}$ or $\mathcal{C}$. The low inlet concentration case (denoted as L in table 1) represents equal inlet concentrations, resulting in a surplus of reactants $\mathcal{B}$ and $\mathcal{C}$.

$\mathcal{A}$, $\mathcal{B}$ and $\mathcal{C}$ react according to

$$\text{Fast reaction:} \quad \mathcal{A} + \mathcal{B} \xrightarrow{k_1} \mathcal{P}$$

$$\text{Slow reaction:} \quad \mathcal{A} + \mathcal{C} \xrightarrow{k_2} \mathcal{Q} \tag{1}$$

(similar to the reaction scheme employed by[2,3,18]) at second-order reaction rates $\omega_1 = k_1 \phi_{\mathcal{A}} \phi_{\mathcal{B}}$ and $\omega_2 = k_2 \phi_{\mathcal{A}} \phi_{\mathcal{C}}$. The reaction rate constants k_1 and k_2 were taken in the ratio 1,000 : 1. Since the reactions are taken to be isothermic, and the fluid velocities are much smaller than the speed of sound everywhere, the use of constant density transport equations (as formulated in the next section) is justified.

For well mixed systems, the ratio between the amount of products formed is completely determined by chemical kinetics, whereas in poorly (diffusion limited) mixed systems local shortages of $\mathcal{B}$ can favor the formation of the slow reaction product $\mathcal{Q}$. The yield of $\mathcal{Q}$ is defined as

$$X_{\mathcal{Q}} = M_{\mathcal{Q}}/M_P \tag{2}$$

where M_j is the mass flux of component j through the cross-section, given by

$$M_j = \int_A \langle u_x \phi_j \rangle dA \tag{3}$$

with u_x being the streamwise velocity component, A denoting the cross-sectional area of the TR, and the brackets representing the ensemble average. The yield may vary from 0.001 in the well mixed regime to 1 for the poorly mixed regime.

The mixing intensity is quantified by the Damköhler number, here defined as the ratio between turbulent macro time scale and the characteristic reaction time scale

Table 1. Damköhler Number $^{10}\log(\mathrm{Da})$ Corresponding to Five (I–V) Reaction Rates for Two Inlet Concentrations $\phi_{\mathcal{A}_0}$ of Reactant $\mathcal{A}$

Case		I	II	III	IV	V
H	$\phi_{\mathcal{A}_0}$=4,000	−4.3	−2.3	−0.3	1.7	3.7
L	$\phi_{\mathcal{A}_0}$= 1	−4.1	−2.1	−0.1	1.9	3.9

$$\mathrm{Da} = \frac{\mathcal{T}}{\mathcal{T}_{\text{reaction}}} \tag{4}$$

For the reaction time scale we take $\mathcal{T}_{\text{reaction}} = (k_2\sqrt{\phi_{\mathcal{A}_0}\phi_{\mathcal{C}_0}})^{-1}$. By choosing different values for k_1 and k_2 (always in the ratio $k_1/k_2 = 1{,}000{:}1$), the Damköhler number was varied over eight orders of magnitude such that a very broad spectrum of mixing regimes is covered. The five Damköhler numbers (indicated as case I–V) are listed in Table 1.

Numerical Simulation Procedure

Transport equations

The state at location $\mathbf{x} \equiv x_i$ ($i = 1, 2, 3$), and time t of any turbulent reactive flow is defined by the local pressure $p(\mathbf{x}, t)$, velocity $\mathbf{u}(\mathbf{x}, t) \equiv u_i$, and scalar composition vector $\boldsymbol{\phi}(\mathbf{x}, t) \equiv \phi_\alpha(\mathbf{x}, t)$, where $\alpha = 1, 2, \ldots, N_s$ refers to the N_s scalar components involved in the set of reactions.[10] For an incompressible, Newtonian fluid, the reacting scalar field is governed by the continuity equation, and the momentum and scalar advection-diffusion equations

$$\nabla \cdot \mathbf{u} = 0 \tag{5}$$

$$\frac{\partial \mathbf{u}}{\partial t} + \mathbf{u} \cdot \nabla \mathbf{u} = -\nabla p + \mathbf{f} + v\nabla^2 \mathbf{u} \tag{6}$$

and

$$\frac{\partial \boldsymbol{\phi}}{\partial t} + \mathbf{u} \cdot \nabla \boldsymbol{\phi} = -\nabla \cdot \mathbf{J} + \boldsymbol{\omega}(\boldsymbol{\phi}) \tag{7}$$

where p is the pressure normalized with the mass density, $\mathbf{f}$ is a body force per unit mass acting on the fluid, v is the kinematic viscosity, $\mathbf{J}$ is the mass flux of the species given by Fick's law of diffusion $\mathbf{J} \equiv J_i^\alpha = -\Gamma \partial \phi_\alpha / \partial x_i$ (where Γ is the scalar diffusivity), and $\boldsymbol{\omega} \equiv \omega_\alpha$ is the reaction rate that usually is a nonlinear function of the local scalar composition array $\boldsymbol{\phi}(\mathbf{x})$. The second equation is generally referred to as the Navier-Stokes (NS) equation.

Large eddy simulation

Within the LES approach, a spatially and temporally invariant low-pass filter operator is applied to the Eqs. 5 and 6 in order to remove the high-frequency fluctuations and, thus, to be able to obtain a numerically feasible solution on a computational grid, coarser than the smallest fluid length scales. The filter operator (denoted as $\langle \cdots \rangle_L$) introduces an additional stress term (approximately $\boldsymbol{\tau}_s = \langle \mathbf{uu} \rangle_L - \langle \mathbf{u} \rangle_L \langle \mathbf{u} \rangle_L$;[24]), which represents the influence of the nonresolved subgrid scale (SGS) velocity fluctuations to the resolved velocity field.[5] assumes an eddy viscosity v_e relating the SGS stress to the resolved strain rate according to $\boldsymbol{\tau}_s = 2v_e \langle \mathbf{S} \rangle_L$. The Smagorinsky eddy viscosity (denoted as $v_{e,S}$), is related to the strain rate modulus $S = \sqrt{(2\mathbf{S}^2)}$, and grid spacing Δ as $v_{e,S} = C_s^2 \Delta^2 S$, where the Smagorinsky constant is a semi-empirical constant.

Although the Smagorinsky model is widely used, its shortcomings are well recognized (for example,[6,25]). In the low mesh Reynolds number limit (that is, when the dissipative scales are close to the grid size), the eddy viscosity in the conventional Smagorinsky model does not approach zero since the resolved strain rate remains finite. Therefore, we use a modified eddy viscosity proposed by[6] according to

$$v_{e,V} = v_{e,S} - \beta v \left[1 - \exp\left(-\frac{v_{e,S}}{\beta v} \right) \right] \tag{8}$$

where $\beta = 2/9$ is recommended. The eddy viscosity given by Eq. 8 correctly approaches zero in the low mesh Reynolds number limit. On top of the Voke modification, also the van Driest's wall damping function[26] is used, which suppresses the eddy viscosity in the wall boundary regions in order to take into account the local reduction in length scales imposed by the wall.

Lattice-Boltzmann LES solver

An efficient solution algorithm for the NS differential equations is provided by the Lattice Boltzmann (LB) solver.[27,28] The LB scheme is based on a very simple microscopic system of fictitious particles that can hop between the sites of a regular lattice and may have collisions only on the lattice sites. Collision rules are chosen such that on a macroscopic level the continuity and Navier-Stokes Eqs. 5 and 6 are recovered. Since the scheme is fully local in nature, it performs very efficiently on parallel platforms; only communication between the adjacent boundaries of neighboring domains is required.

An adaptive forcing technique[7] is used to impose the flow boundary conditions. The technique describes the geometry by a set of M control points on the boundary lying inside the uniform, cubic LB grid. At the control points, a force is dynamically adjusted such that prescribed velocities are maintained. At the tube and injector walls a zero slip velocity is imposed, while at the injection point a fixed velocity is set at a single grid point located in the injector exit. In this way, a momentum point source rather than a well defined jet flow is imposed. We, hence, expect some resolution problems in the jet exit regions, although further downstream the resolution requirements are relaxed due to entrainment of ambient fluid from the main flow. Periodic boundary conditions are applied in streamwise direction to sustain a developed turbulent flow at the inlet. The length of the reactor tube was taken ten reactor diameters in order to ensure that the influence of the feed pipe at the inlet was minimal. This assumption will be checked in

the result section. The main flow is driven by a uniform body force that is applied to the whole flow domain. The body force is dynamically adjusted such that the momentum flow through the reactor is kept constant (which otherwise would increase due to the jet).

Filtered density function

Just treating the scalar advection-diffusion Eq. 7 in the LES context (that is, on the analog of the SGS stresses) is not appropriate due to the lack of information about the joint distribution of the reacting species on subgrid scale level, which is required to determine the filtered reaction rate $\boldsymbol{\omega}$ in case of second and higher order reactions.[10] Rather, a transport equation for the joint probability density function of the LES filtered scalar quantities (the filtered density function (FDF)) is formulated[13,14]

$$\frac{\partial P_L}{\partial t} + \langle \mathbf{u} \rangle_L \cdot \nabla P_L = -\nabla \cdot [(\langle \mathbf{u} | \boldsymbol{\psi} \rangle_L - \langle \mathbf{u} \rangle_L) P_L] + \frac{\partial}{\partial \psi_\alpha} \left\{ \left[\left\langle \frac{\partial J_i^\alpha}{\partial x_i} \middle| \boldsymbol{\psi} \right\rangle_L - \hat{\omega}_\alpha(\boldsymbol{\psi}) \right] P_L \right\} \quad (9)$$

where $\langle X | Y \rangle_L$ denotes the filtered value of X conditioned on Y, $\boldsymbol{\psi}$ is the value in composition space of the scalar quantity $\boldsymbol{\phi}$, and the summation convention applies to both species suffix α and the coordinate suffix i. The FDF P_L can formally be defined as

$$P_L(\boldsymbol{\psi}; \mathbf{x}, t) = \int_{-\infty}^{\infty} \rho(\boldsymbol{\psi}, \boldsymbol{\phi}(\mathbf{x}', t) G(\mathbf{x}' - \mathbf{x}) d\mathbf{x}' \quad (10)$$

$$\rho[\boldsymbol{\psi}, \boldsymbol{\phi}(\mathbf{x}, t)] = \delta[\boldsymbol{\psi} - \boldsymbol{\phi}(\mathbf{x}, t)] \equiv \prod_{\alpha=1}^{N_s} \delta[\psi_\alpha - \phi_\alpha(\mathbf{x}, t)] \quad (11)$$

where δ is the Dirac delta function, $\rho[\boldsymbol{\psi}, \boldsymbol{\phi}(\mathbf{x}, t)]$ is known as the fine-grained density[29] and $G(\mathbf{x})$ is the low-pass filter corresponding to the LES filter operator $\langle \cdots \rangle_L$.

An LES must be used to supply the resolved scale velocity $\langle \mathbf{u} \rangle_L$. Equation 9 describes the change of the FDF P_L due to several processes. The convection term (second term on the l.h.s.) and chemical reaction term (last term on r.h.s.) are closed (and, thus, do not need any modeling). The terms that need closure are the unresolved SGS convection and diffusion term, given by the first and second term on the r.h.s., respectively.

An eddy viscosity model is adopted for the FDF SGS convective flux

$$[\langle \mathbf{u} | \boldsymbol{\psi} \rangle_L - \langle \mathbf{u} \rangle_L] P_L = -\Gamma_e \nabla P_L, \quad (12)$$

where Γ_e is the eddy scalar diffusivity related to the eddy viscosity through the turbulent Schmidt number: $\Gamma_e = \nu_e / Sc_t$.

The SGS diffusion term can be decomposed into a part which represents transport in physical space and a part which represents transport in composition space

$$\frac{\partial}{\partial \psi_\alpha} \left[\left\langle \frac{\partial J_i^\alpha}{\partial x_i} \middle| \boldsymbol{\psi} \right\rangle_L P_L \right] = \nabla \cdot \Gamma \nabla P_L - \frac{\partial^2}{\partial \psi_\alpha^2} [\langle \chi_\alpha | \boldsymbol{\psi} \rangle_L P_L] \quad (13)$$

where $\chi_\alpha = \Gamma \nabla \phi_\alpha \cdot \nabla \phi_\alpha$ represents the scalar energy dissipation rate of component α. The conditional scalar energy dissipation rate $\langle \chi | \boldsymbol{\psi} \rangle_L$ takes care of the diffusion in composition space, and needs to be modeled. Note that the latter diffusion term is negative, and therefore exhibits behavior opposite to the diffusion of a scalar quantity in physical domain; instead of being smoothed, gradients in compositional domain are steepened toward a final equilibrium state of an impulse at the scalar average.

The "interaction by exchange with the mean" (IEM) model[29] is a simple closure that assumes (originally referred to by[29] as "least mean square estimation" (LMSE) model)

$$-\frac{\partial^2}{\partial \psi_\alpha^2} [\langle \chi_\alpha | \boldsymbol{\psi} \rangle_L P_L] = \frac{\partial}{\partial \psi_\alpha} [\Omega_m [\psi_\alpha - \langle \phi_\alpha \rangle_L] P_L] \quad (14)$$

Here, Ω_m represents the frequency of mixing within the subgrid, which is related to the subgrid diffusion coefficient and the filter length

$$\Omega_m = C_\Omega (\Gamma + \Gamma_e) / \Delta_G^2 \quad (15)$$

where $C_\Omega = 3$ (due to[15]).

Algorithm 0.1 Monte Carlo solution of FDF equation (16)

Read initial flow field $\mathbf{u}(\mathbf{x}, t_0)$
Read initial Monte Carlo particles (MCP) $\boldsymbol{\phi}(\mathbf{X}^+, t_0)$
for $n = 1, 2 \cdots$ number of timesteps **do**
  Update LES flow field $\langle \mathbf{u}(\mathbf{x}), t_n \rangle_L$
  Interpolate flow properties to MCP
  Calculate drift and diffusion at MCP (Eq. 20)
  Step MCP in physical space (eq. 17)
  Update $\langle \boldsymbol{\phi}(\mathbf{x}, t_n) \rangle_L$ from MCP
  Calculate scalar drift coefficient (eq. 21)
  Update MCP $\boldsymbol{\phi}^+(\mathbf{X}^+, t_n)$ (eq. 18)
  Deal with the boundary conditions
end

With the closures given by Eqs. 12 and 14 the modeled FDF transport equation is

$$\frac{\partial P_L}{\partial t} + \langle \mathbf{u} \rangle_L \cdot \nabla P_L = \nabla \cdot [(\Gamma + \Gamma_e) \nabla P_L] + \frac{\partial}{\partial \psi_\alpha} [\Omega_m (\psi_\alpha - \langle \psi_\alpha \rangle_L) P_L] - \frac{\partial}{\partial \psi_\alpha} [\hat{\omega}_\alpha(\boldsymbol{\psi}) P_L] \quad (16)$$

The closures used in this formulation are essentially the same as[15] used for the 2-D mixing layer.

FDF solver

The modeled FDF transport Eq. 16 gives a full statistical description of the filtered scalar composition field. The first moment is equivalent to the equation that can be obtained by

low pass filtering the scalar advection-diffusion Eq. 7. In the FDF formulation, modeling of the reaction term is not required since it remains closed.

A finite difference solution of FDF transport equation is not feasible, since the computational demands grow exponentially with the dimension (that is, the number of species N_s) of the system. For high-dimensional systems, a Lagrangian Monte Carlo (MC) solver turns out to be more efficient.[10] The idea of the MC method is to release computational particles randomly into the computational domain. Each particle represents the scalar composition $\boldsymbol{\phi}^+$ at its current position $\mathbf{X}(t)$. The MC particle position and composition are evolved according to the stochastic differential equations (SDE)

$$d\mathbf{X} = \mathbf{D}(\mathbf{X}(t), t)dt + E(\mathbf{X}(t), t)d\mathbf{W}(t) \tag{17}$$

and

$$d\boldsymbol{\phi}^+ = \mathbf{B}(\boldsymbol{\phi}^+(t))dt \tag{18}$$

where $\mathbf{D}$ and E are the drift and diffusion coefficients of the particles in the physical domain, $d\mathbf{W} \equiv dW_i = (dt)^{1/2}\xi_i$ is a Wiener process [with ξ_i a random variable with standard Gaussian PDF];[10], and $\mathbf{B} \equiv B_\alpha$ denotes the drift in scalar domain due to micromixing and chemical reactions. The FDF transport equation corresponding to the SDE Eq. 17 and Eq. 18 is

$$\frac{\partial P_L}{\partial t} = -\nabla \cdot (\mathbf{D}P_L) + \frac{1}{2}\nabla^2[E^2 P_L] - \frac{\partial}{\partial \psi_\alpha}(B_\alpha P_L) \tag{19}$$

A comparison of this Fokker-Planck equation with the modeled FDF transport Eq. 16 shows that the two systems are equivalent for a particular specification of the drift and diffusion coefficients, viz

$$E = \sqrt{2(\Gamma + \Gamma_e)} \quad \text{and} \quad \mathbf{D} = \langle \mathbf{u} \rangle_L + \nabla(\Gamma + \Gamma_e) \tag{20}$$

respectively, and for the scalar drift coefficient

$$\mathbf{B} = -\Omega_m(\boldsymbol{\phi}^+ - \langle \boldsymbol{\phi}^+ \rangle_L) + \hat{\boldsymbol{\omega}}(\boldsymbol{\phi}^+(t)) \tag{21}$$

The solution procedure is given in algorithm 0.1. Linear interpolation is used to obtain the flow properties at the MCP. The boundary conditions are set at the inflow of the main tube and the jet. In order to attain a uniform particle density over the cross-section of the inlet to the reactor tube, every time step the boundary grid cells are filled with MC particles up to a prescribed particle density N_0.

Practical aspects

The flow in the tubular reactor was calculated on a 800×83^2 cubical computational grid with unity grid spacing Δ. At the wall of this domain, free slip boundary conditions were imposed, except for the inlet and outlet, where periodic boundary conditions were taken. The outer tube wall had a diameter of 80Δ, and was defined by 220,635 control points, whereas the feed pipe diameter of 16Δ was defined by 5,787 control points. A circular hole in the feed pipe of 4Δ in diameter was defined. In the center of the hole, the jet flow was driven by a momentum source imposed on a single grid point.

The speed of sound in the LB framework is about one, implying that $|\mathbf{u}|^2 \ll 1$ in order to keep the flow within the incompressible limit. The jet velocity was fixed at $u_j = 0.16$ (from here on, all quantities are specified in LB units) compared to 0.64 m/s in the physical equipment. The bulk flow was driven by a body force f_0 that was dynamically adjusted via the mass outflow in order to keep a fixed mean velocity (without this adjustment, the bulk velocity would increase due to the momentum imparted by the jet). In this way, a mean velocity of 0.01 in the tube was established (compared to 0.04 m/s in the physical equipment). A Reynolds number of 4,000 (which was chosen in agreement to the flow condition of the 3D-LIF experiment of 22) was obtained by choosing a kinematic viscosity of $\upsilon = 2.0 \times 10^{-4}$. The LB solver requires to store 22 (18 directions, 3 force components and one eddy viscosity) single-precision values on every grid node, resulting in a total memory requirement of approximately 0.45 GB.

The estimate of υ combined with a molecular Schmidt number of $\mathrm{Sc} = 2{,}000$ leads to a molecular diffusivity of $\Gamma = \upsilon/\mathrm{Sc} = 1.0 \times 10^{-7}$. The choice for the semi-empirical Smagorinsky constant was $C_s = 0.12$ (due to[7]). The turbulent Schmidt number relating the eddy diffusivity Γ_e to the eddy viscosity υ_e was set to $Sc_t = 0.7$. This choice establishes a dissipation of the nonresolved scalar fluctuations larger than the nonresolved velocity fluctuations. It was argued by,[18] however, that one single time scale relating the dissipation of both spectra is probably not sufficient due to the distinct behavior of the high frequency part of the scalar power spectrum compared to the kinetic energy power spectrum. This aspect will be discussed in the results section.

The FDF solver is computationally more expensive than the LB-LES solver, and requires a larger amount of memory. In order to limit the computational effort of the reactive scalar, only the first half of the flow domain was employed; resulting in a $400 \times 83 \times 83$ grid containing 20 Lagrangian MC particles per grid cell on average. Each particle represented the full composition array of the five scalar components of five independent reaction schemes of varying Damköhler numbers (see table 1), so that in a single run several cases were calculated. Every MC particle required 36 single-precision real values to be stored (25 for the reacting scalar components, one for the nonreacting scalar, three for the position, three for the velocity, one for the eddy viscosity, and three for the gradient vector of the eddy viscosity), resulting in a total memory requirement for the FDF solver of $400 \times 83^2 \times 20 \times 36 \times 4 \approx 7.4$ GB plus about 0.3 GB to store the Eulerian scalar field.

The code was implemented on a Linux cluster of ten dual AMD Athlon(TM) MP 1800+ processors and one dual Pentium III 500 MHz processor with a total amount of 11 GB of distributed memory. The ten AMD processors took care of FDF scalar solver, whereas the part of flow domain without scalars was solved on the slower Pentium III node. It took about 1.5 day to calculate one macro time scale D_t/U_m (8000 LB time steps). For an initial distribution, it took about a week to obtain a steady flow, and the statistics were obtained from about 20 macro time scales (taking about a month for each run). For the simulations discussed in this article, the parallel computer cluster was kept busy for almost three months.

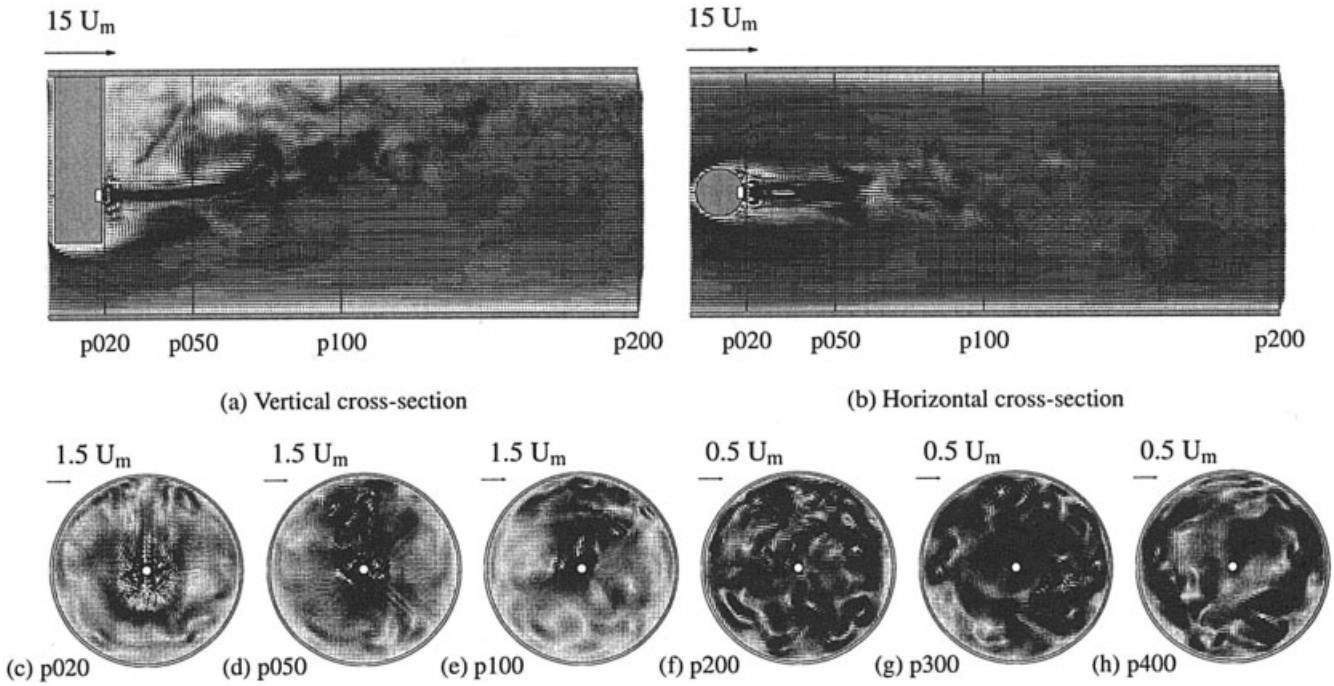

Figure 2. Instantaneous velocity field in a vertical (a), and horizontal (b) center line plane, and six flow-normal vertical planes (c–j) corresponding to the positions p020–p400.

Results

Below, the results of the FDF simulation in the TR will be presented. It has already been mentioned that within the FDF approach the reaction term remains closed, and modeling applies to the SGS mixing of the scalars only. Therefore, first of all, the mixing of a nonreacting conserved scalar (denoted as $\mathcal{S}$) replacing reactant $\mathcal{A}$ is studied and compared to the measurements described in the previous section. The mixing of the reactive scalars of the parallel competitive reaction system described earlier, will be presented next.

Conserved scalar mixing

First, some instantaneous results are presented to get qualitative pictures of the flow, and the conserved scalar transport in the TR. Next, a spectral analysis has been performed to gain insight in the turbulent characteristics of the flow. Then, the averaged conserved scalar concentration is compared to experimental 2D-LIF results. Finally, the performance of the FDF/LES model is assessed by comparing the concentration PDF's with experimental LIF data.

Instantaneous Realizations. Impressions of the instantaneous turbulent velocity field and the conserved (nonreacting), passive scalar concentration field are given in Figures 2 and 3, respectively. The velocity vector plot of Figure 2 shows that a turbulent wake is formed downstream of the injector. In this wake, the jet at the exit of the injector is visible. In the vertical side view (Figure 2a), it is shown that the jet is inclined upwardly promoted by the main stream flowing around the blockage formed by the feed pipe. Turbulent structures are formed and recirculation occurs. The yz-planes (coordinate definition in Figure 1b normal to the stream direction (Figure 2c–h) show the downstream development of the transverse velocity field.

The conserved scalar field shown in Figure 3 exhibits the same features as a flow field: an upwardly inclined jet in a turbulent wake. The flow-normal yz-planes (Figure 3c–h) illustrate that the dye close to the feed pipe resides in the wake. The recirculation and low velocities in the wake of the injector cause the dye to be distributed over the whole length of the feed pipe. This is most clearly visible in the flow-normal yz-plane (Figure 3c). The dye outside the wake is advected immediately away due to the larger velocity of the main stream. Further downstream, the dye is taken to the top of the reactor (from position p100 at $x/D_t = 0.10$), where it is directed along the outer wall of the tube. After position p300 (at $x/D_t = 3.5$), the dye reenters the central horizontal plane at both sides of the reactor.

For the flow around an infinitely long circular cylinder at $Re_f = 800$, vortex shedding occurs in the "irregular" regime, with vortices that become turbulent in themselves.[23] In the tubular reactor the flow is more complex; the feed pipe cannot be considered infinitely long, and a jet is injected into its wake. Even so, the horizontal cross-section view of the concentration field (Figure 3b) suggests that vortices at regular distances are formed in the tubular reactor. Earlier in this article, it was estimated that in this particular flow geometry, the time $\mathcal{T}_v$ between the shedded vortices happens to be equal to the macro time scale $\mathcal{T}$. This implies that the distance between the successive vortices should be of the order of a reactor dia. D_t. This is roughly confirmed by the location of the vortices in Figure 3b: the distance between two consecutive vortices (indicated by A and C) is about D_t.

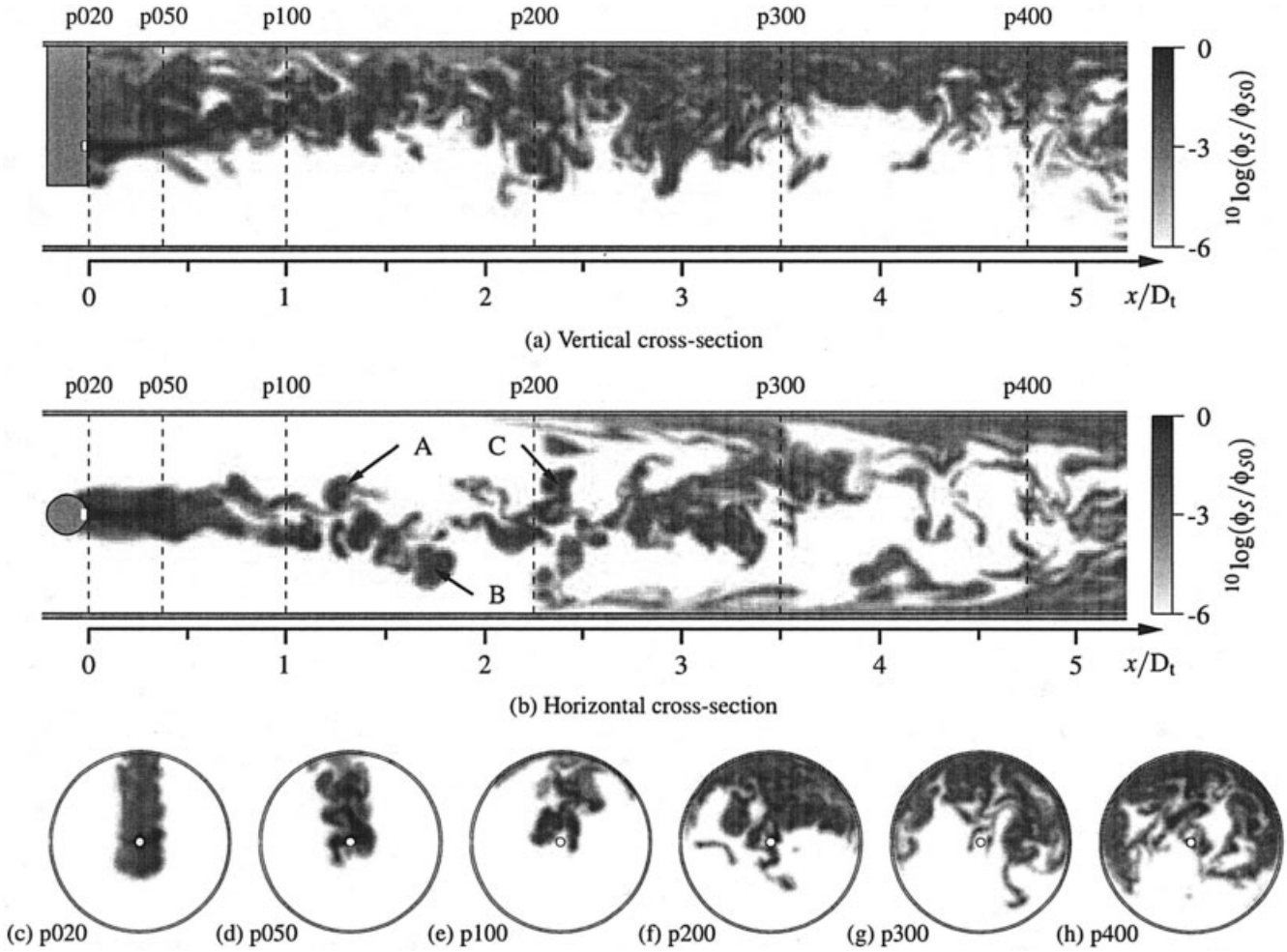

Figure 3. Instantaneous conserved scalar field (same planes as Fig. 2).

Labels A–C indicate shedded vortices. A log scale is used to pronounce the low scalar values with respect to the inlet concentration.

Time Series and Spectral Analysis. Time series of the spanwise velocity component u_y at three downstream positions are shown in Figure 4. While the first position is at the injector opening (Figure 4a), the second position is at $x/D_t = 1.0$ in the wake close to the injector (Figure 4b), and the last position is at $x/D_t = 7.6$ far downstream (Figure 4c). The power spectral density functions corresponding to the time series are shown in Figure 5. The angular frequency is denoted as $\Omega = 2\pi/T$, where T is the time. In the LB framework, the time resolution

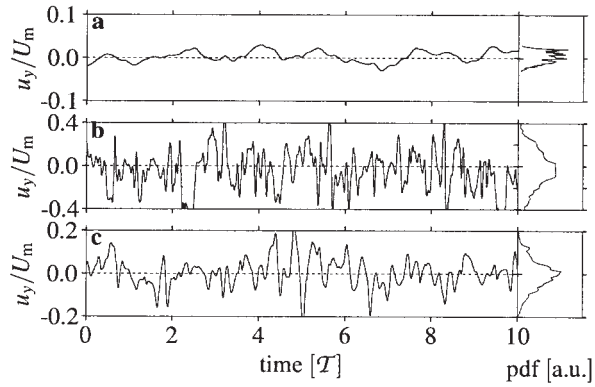

Figure 4. Time series captured at three downstream center line positions $x/D_t = 0.0$ (a), $x/D_t = 1.0$ (b) and $x/D_t = 7.6$ (c).

The PDF's are obtained from 25 macro time scales.

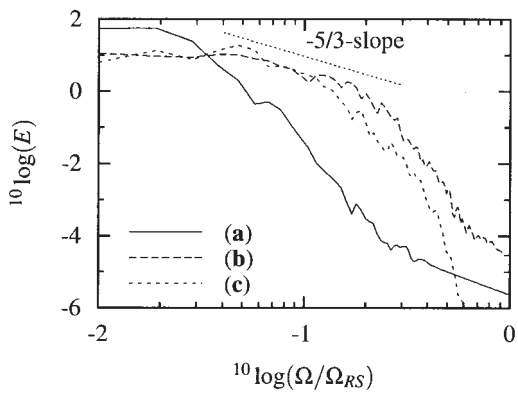

Figure 5. Normalized power spectral density functions corresponding to the time series shown in Figure 4.

is much higher than the space resolution.[27] The highest frequency contribution in a time series is due to the advection of the smallest resolved spatial scale $\Delta x/U_m$. The angular frequency Ω_{RS} corresponding to this time scale is used to normalize the frequency domain.

The transverse velocity fluctuations at the jet exit are suppressed. The power spectral density function falls off very rapidly, and does not show any turbulent characteristics. In the wake (b) at $x/D_t = 1$, the turbulent fluctuations are most intense (note the different vertical-scales of Figure 4a–c). At this position, the widest range of turbulent scales is found and a small inertial $-5/3$-range is recognized. At the far downstream position $x/D_t = 7.6$, the fluctuation intensity is weaker again, and the power spectral density hardly shows any inertial range, which reflects the weak turbulence in a tube flow with $Re = 4{,}000$.

Although vortex shedding is found in the instantaneous concentration field shown in Figure 3b, this is not visible in the power spectral density function. It has already been mentioned that vortex shedding was in the irregular regime, and, consequently, no truly fixed shedding periodicity is expected. On top of that, the Strouhal frequency of the feed pipe coincides with the energy-rich turbulent macro time scales, which makes it hard to distinguish the energy contribution of the Strouhal oscillations to the power spectrum.

The time and spectral analysis shows that in spite of the relatively low Reynolds number $Re_m = 4{,}000$, the flow is moderately turbulent. Especially in the wake close to the feed pipe, an inertial range is formed and turbulence is generated. At the far downstream position, the low-mesh Reynolds number modification (Eq. 8) of the eddy viscosity model is required.

Average Concentration: Comparison to 2D-LIF Experiments. In Figure 6, the average concentration in a vertical and horizontal central plane (obtained from 20 macro time scales) is depicted and compared to experimental results of 2D-LIF measurements (obtained from the work reported by).[22] The numerical result shows the mean concentration extending over a range of about six orders of magnitude. To depict such a large signal range, the concentration was put on a log scale. The signal range of the experimental concentration measurement was only two orders of magnitude, due to the limited signal to noise ratio of the 255-bit CCD camera. In order to compare the experimental to the numerical result, the same log scale was used. It should be stressed, however, that no concentration values lower than $^{10}\log(\zeta/\zeta_0) = -2.5$ could be measured due to the limited signal to noise ratio of the CCD camera. Furthermore, it should be kept in mind that in the complex flow investigated in this article, it is hard to obtain statistical convergence, and 20 macro time scales may not be sufficient to draw strong quantitative conclusions.

The experimental and numerical result show qualitative agreement. The vertical cross-section of both the numerical (Figure 6a) and the experimental result (Figure 6c) show an upwardly inclined jet that reaches the top of the reactor tube at about $x/D_t = 1.5$. From there on the dye moves mainly along the upper part of the reactor tube. In the numerical result, the dye profile broadens over the tube height further downstream. The concentration in the lower part of the reactor remains orders of magnitude lower than the upper part. Since the signal range of the experiment was low, the concentrations in the lower part of the reactor were too low to be measured, and, consequently, this broadening could not be observed.

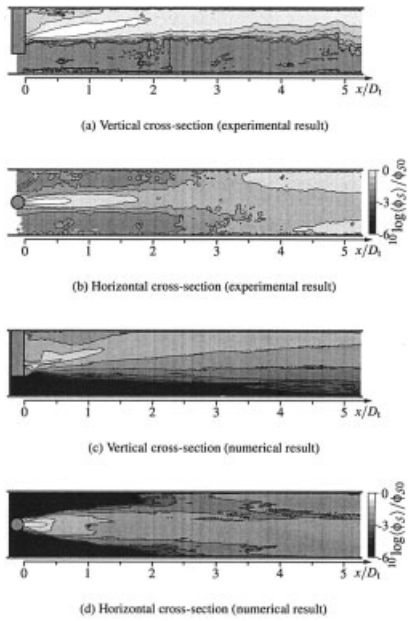

Figure 6. Experimental (top) and numerical (bottom) results of the mean, conserved scalar concentration in a vertical (left) and horizontal (right) center plane.

The experimental results are described in detail in Van Vliet et al.[22]

The horizontal cross-sections in Figure 6b and 6d show that in both results the jet leaves the horizontal plane between $x/D_t = 1 \sim 2$, and that the dye abruptly reenters the plane at the sides of the tube at about $x/D_t = 2.5$.[22] suggested that the dye is advected with the flow along the tube wall. The instantaneous concentration fields of the flow-normal yz-planes 3c–h seem to confirm this explanation.

Although a qualitative agreement of the average dye transport between the experiment and the numerical simulation is obtained, major differences occur in the region close to the feed pipe. In the experiment, the higher concentration values penetrate deeper into the reactor, whereas in the numerical simulations the scalar concentration only attains its initial value immediately after the exit. This could well be attributed to the resolution problems nearby the exit of the jet mentioned before. This aspect is discussed in more detail later.

Assessment of the FDF/LES Model. The experimentally and numerically obtained concentration PDF's determined at six downstream positions (indicated by p020, p050, p100, p200, p300, and p400 in Figures 2 and 3) are shown in Figures 7a and 7b respectively. At the first measuring position ($x/D_t = 0.5$), the concentration distribution of the experimental result (Figure 7a) covers the whole domain, including the initial concentration of the unmixed dye, whereas the highest values in the distribution at the same position of the numerical result have already decayed to $\phi = 0.9$. From $x/D_t = 1.0$, the numerical concentration PDF's relax to an equilibrium, whereas in the experiment this equilibrium is established only after $x/D_t = 3.5$ (the experimental PDF's in the range $x/D_t =$

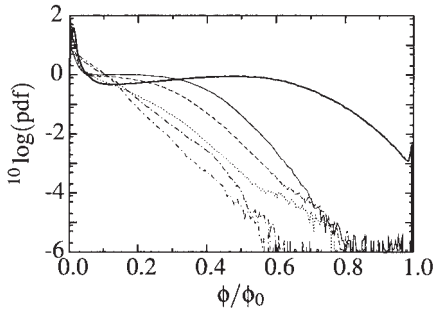

(a) Experimental result

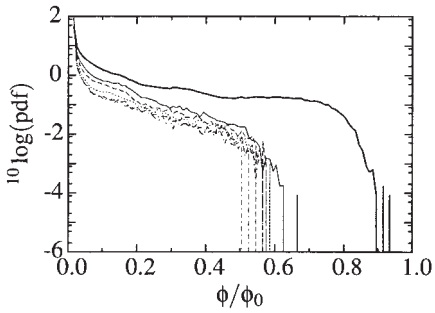

(b) Numerical result

Figure 7. Numerical and experimental downstream evolution of the concentration pdf of the nonreacting scalar at positions x/D$_t$: 0.5 (bold); 1.0 (solid); 1.5 (dashed); 2.5 (dotted); 3 (long dash-dot); 4.5 (short dash-dot).

$5.5 \sim 6.5$ are not shown, but are more or less the same as the PDF at $x/D_t = 4.5$).

The mean and the variance obtained from the concentration PDF's are depicted in Figures 8a and 8b. The variance is normalized with $\langle\phi\rangle[1 - \langle\phi\rangle]$, that is, the upper bound variance associated to a completely segregated binary mixture (see for example[30]). In Figure 8a, it is shown that the mean is underpredicted, consistent with the excessive spreading of the scalar mean as illustrated in the previous paragraph by Figure 6. Figure 8b shows that in the vicinity of the feed pipe (at $x/D_t = 0.0$), the normalized variance is close to the upper bound of one (that is, the mixture is almost completely segregated). Further downstream, the decreasing normalized variance shows that micro mixing is becoming more and more active. A comparison to the experimental results shown in the same graph indicates that the FDF/LES model underpredicts the variance in the first part of the reactor (up to $x/D_t \approx 4$), meaning that micro mixing in this region is overpredicted. Further downstream, after about $x/D_t = 4$, both the mean and the variance predicted by the FDF/LES model are consistent with the experiments.

The overprediction of the mean spreading of the scalar field may be caused by an overprediction of either (1) the LES velocity fluctuations or (2) the FDF SGS flux (due to the second term on the l.h.s., and the first term on r.h.s. of Eq. 9, respectively). In the vicinity of the jet exit, a transition region exists of the laminar jet entraining into the turbulent wake of the feed pipe. Such transition regions are not properly captured by the Smagorinsky eddy viscosity model, since this model assumes a local balance between production and small scale dissipation. In this particular region, the eddy viscosity is, therefore, likely to be overestimated, since the local reduction in length scales is not taken into account. Since an overestimated eddy viscosity contributes to the suppression of the LES velocity fluctuations, we do not expect that mechanism (1) is responsible for the excessive spreading of the jet. This assumption is consistent with the suppressed velocity fluctuations and the non-developed turbulent power spectral density function found in the jet exit region, as was shown in figure 4. Mechanism (2) (the FDF SGS flux), however, is proportional to the turbulent diffusivity (through the drift and diffusion in Eq. 20), promoting the turbulent diffusion length l_t with respect to molecular diffusion length l as $l_t/l \sim \sqrt{\Gamma_e/\Gamma} = \sqrt{(v_e/v)} \cdot \sqrt{(Sc/Sc_t)}$. In our case, $v_e/v \approx 10$ in the exit of the jet. On top of that, the assumed constant turbulent Schmidt number $Sc_t = 0.7$ is adequate for a fully developed scalar spectrum only, and may lead to overprediction of turbulent diffusivity in the vicinity of the scalar source (that is, in regions where the scalar spectrum has not developed yet) proportional to $\sqrt{Sc/Sc_t} \approx \sqrt{3{,}000}$. The inappropriate turbulence modeling in a laminar environment, hence, may lead to an overprediction of Γ_e up to two orders of magnitude, and likely is the cause of the excessive spreading of the jet via the overpredicted SGS flux.

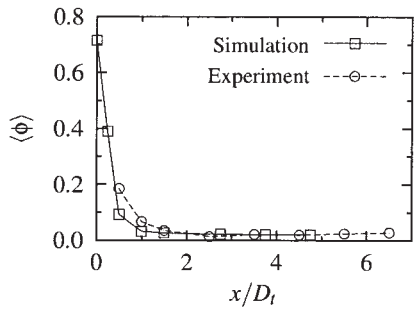

(a) Mean

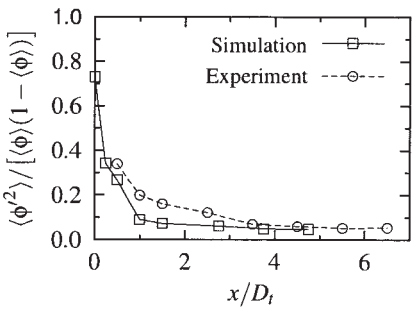

(b) Normalized variance

Figure 8. The mean concentration, (a) and its variance normalized with the upper bound variance $\langle\phi\rangle(1 - \langle\phi\rangle)$; (b) obtained from the concentration pdf's shown in Figure 7 against the distance downstream the injector.

The overprediction of the mixing rate (observed as an excessive decay of scalar variance in Figure 8b) may also be the result of the overprediction of the turbulent diffusivity, leading to an over prediction of the mixing frequency given by Eq. 15, and consequently, to an overprediction of scalar energy dissipation rate by the IEM micro mixing model (Eq. 14). Note that this overprediction is not a feature of the IEM model, but rather a result of an inaccurate estimate of the mixing frequency.

Some Concluding Remarks. So far, we have shown that the macro transport of a passive scalar is qualitatively reasonably well predicted by the FDF/LES model: macro flow characteristics are recovered satisfactorily, and the distribution of the dye over the height of the reactor was consistent with experimental results. An overprediction of the decay of the scalar mean and variance in the vicinity of the injector was attributed to the over prediction of the turbulent diffusivity in the laminar to turbulent transition region of the jet, leading to an overprediction of the SGS flux. It was shown, however, that these effects were mainly confined to the first part of the reactor up to $x/D_t = 3.5$, and that from there on both experimental and numerical results established a more or less similar equilibrium state. We, therefore, expect that for simple reactions, the FDF/LES model used in the present research is adequate for correctly predicting the selectivity.

Reactive scalar mixing

Now, the reactive system for several Damköhler numbers and two inlet concentrations (see table 1) is studied.

Instantaneous Consumption and Production. An image of the instantaneous concentration field of the fast reactant $\mathcal{B}$ and slow product $\mathcal{Q}$ for a poorly (a and c) and well (b and d) mixed system is given in Figure 9 for the high inlet concentration case. Reactant $\mathcal{B}$ enters the reactor at its initial concentration ($\phi_{\mathcal{B}} = 1$), gets into contact with the feed stream $\mathcal{A}$ in the jet region, and is converted into $\mathcal{P}$. Simultaneously, the slow reactant $\mathcal{C}$ is converted into the slow product $\mathcal{Q}$. In the poorly mixed system, the turbulent time scales are much larger than reaction time scales, and reactant $\mathcal{B}$ is consumed almost instantaneously (shown in Figure 9a). As a result, sharply defined regions are formed of either $\phi_{\mathcal{B}} = 0$ (black), or $\phi_{\mathcal{B}} = 1$ (white). Due to the local shortage of the fast reactant $\mathcal{B}$ in the black regions, also the slow reactant $\mathcal{C}$ can be completely converted, resulting in a high yield of product $\mathcal{Q}$ with also an almost complete binary distribution (Figure 9c).

In the well mixed system, the reaction time scales are much larger compared to the turbulent time scales. During the reaction, molecular and turbulent scalar diffusion occurs also, which is reflected by the smoothly varying concentration field of the fast reactant $\mathcal{B}$ shown in Figure 9b. Moreover, no local shortage of reactant $\mathcal{B}$ is formed, and the slow reaction of $\mathcal{C}$ into $\mathcal{Q}$ is hardly taking place. As a result, hardly any product $\mathcal{Q}$ is formed (notice that in Figure 9c pure black corresponds to $\phi_{\mathcal{Q}} = 1 \times 10^{-3}$). Small spots with relatively high concentration of $\mathcal{Q}$ are formed in the downstream direction.

For the low initial concentration $\phi_{\mathcal{A}0} = 1.0$ (case L in table 1), the instantaneous realizations have the same features as the high concentration close to the feed pipe (not shown in a figure). From about $x/D_t = 1.0$, however, all reactant $\mathcal{A}$ has reacted away. As a result, no products are formed anymore, and the concentration fields of all species are smoothed by turbulent and molecular diffusion.

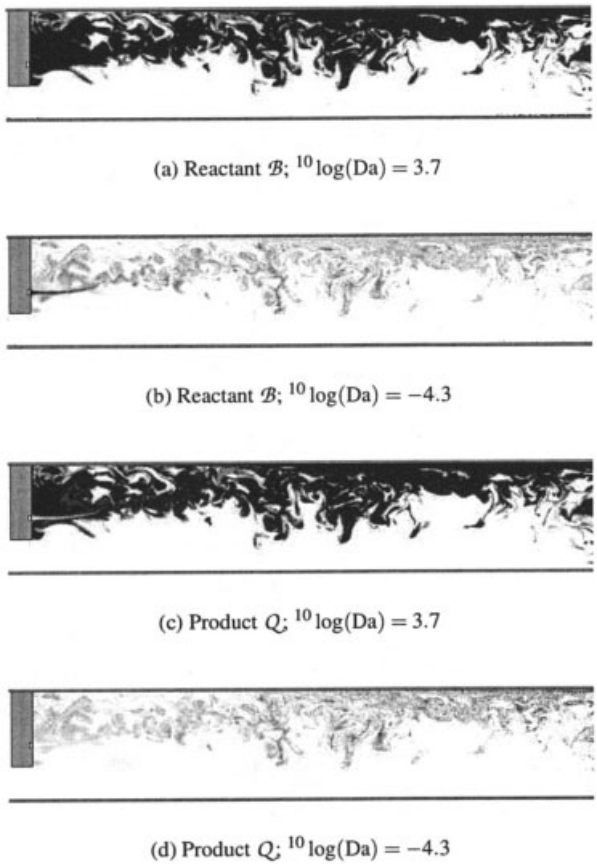

Figure 9. Comparison of vertical cross-section view of a poorly (a and c) and a well (b and d) mixed system in terms of fast reactant $\mathcal{B}$ and slow product $\mathcal{Q}$ for the high inlet concentration $\phi_{\mathcal{A}0} = 4{,}000$.

The reactant $\mathcal{B}$ is depicted on a linear gray scale ranging between $\phi_{\mathcal{B}} = 0$ (black) and $\phi_{\mathcal{B}} = 1$ (white). The product $\mathcal{Q}$ is represented by a linear gray scale ranging between white ($\phi_{\mathcal{Q}} = 0.0$) and black, where pure black corresponds to $\phi_{\mathcal{Q}} = 1$ for the poorly mixed system (c) and to $\phi_{\mathcal{Q}} = 1 \times 10^{-3}$ for the well mixed system (d).

Composition Distribution. A more quantitative idea of the product distribution is obtained by the PDF's shown in Figure 10, where each picture shows the distributions of all scalar components over the entire cross-section. A comparison for different inlet concentrations, downstream positions, and Damköhler numbers is made.

In Figure 10a–d, the high inlet concentration of reactant $\mathcal{A}$ is considered (case H in Table 1). Since there is a surplus of $\mathcal{A}$, its total consumption relatively to the initial mass input is negligible for every Damköhler number, and as a consequence, the distribution of both the high and low Damköhler number cases approaches the passive scalar distribution presented earlier in Figure 7. For the large Damköhler number (Figure 10a and 10b), the consumed reactants $\mathcal{B}$ and $\mathcal{C}$ and the formed product $\mathcal{P}$ and $\mathcal{Q}$ show the same bimodality as observed in the instantaneous realizations shown in Figure 9a; due to the short reaction time scales compared to the turbulent time scales, $\mathcal{B}$

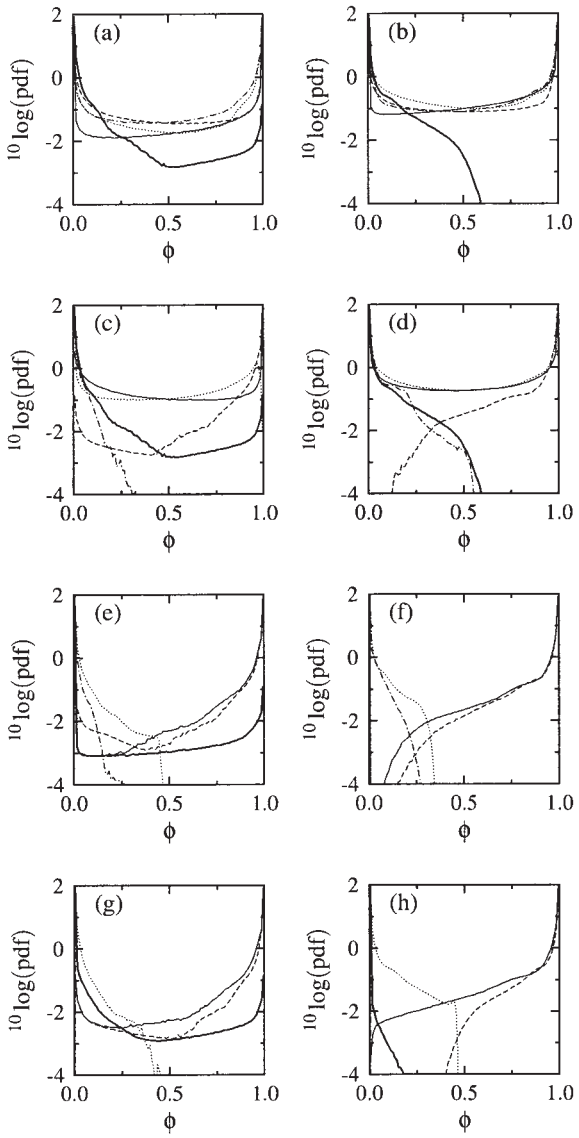

Figure 10. Concentration PDF of reactants and products over the cross-section at a close (a, c, e, g) and far (b, d, f, h) downstream position for a large (a, b, e, f) and small (c, d, g, h) Damköhler number and a high (a–d) and low (e–h) inlet concentration, with values $\phi_{\mathcal{A}0}$ – x/D_t – ^{10}log Da: (a) 4,000 – 0.0 – 3.7; (b) 4,000 – 4.75 – 3.7; (c) 4,000 – 0.0 – −4.3; (d) 4,000 – 4.75 – −4.3; (e) 1.0 – 0.0 – 3.9; (f) 1.0 – 4.75 – 3.9; (g) 1.0 – 0.0 – −4.1; (h) 1.0 – 4.75 – −4.1.

The species are represented by: $\mathcal{A}$, bold solid line; $\mathcal{B}$, normal solid line; $\mathcal{C}$, dashed line; $\mathcal{P}$, dotted line; $\mathcal{Q}$, dash-dot line.

and $\mathcal{C}$ are completely converted into $\mathcal{P}$ and $\mathcal{Q}$ as soon both streams are brought into contact. For the small Damköhler number (Figure 10c and 10d), only the distribution of the species of the fast reaction ($\mathcal{B}$ and $\mathcal{P}$) remain bimodal. The distributions of the species of the slow reactions ($\mathcal{C}$ and $\mathcal{Q}$) diffuse into composition space and lose their bimodality due to reaction time scales being long compared to the turbulent timescales. This reflects the smoothly varying instantaneous concentration field shown in Figure 9. The small high $\mathcal{Q}$ concentration spot mentioned earlier are now reflected in the broadening of the product distribution in Figure 10d compared to 10c.

The case with the low inlet concentration of reactant $\mathcal{A}$ (case L in Table 1) is considered in Figure 10e–h. The distribution of $\mathcal{A}$ now shows a clear difference with the former case. Again, at the close downstream position (Figure 10e and 10g) a bimodal distribution is found with large peaks on $\phi_{\mathcal{A}} = 0.0$ and $\phi_{\mathcal{A}} = 1.0$. In contrast to case H, however, at the far position reactant $\mathcal{A}$ has now almost completely reacted away; only in the low Damköhler case (Figure 10g), a small remainder of low concentration values of $\mathcal{A}$ is left. Since scalar $\mathcal{A}$ now is the limiting reactant, the formed products $\mathcal{P}$ and $\mathcal{Q}$ never show the bimodality as found in case H, but have a peak at zero that broadens to higher values further downstream.

Product Formation and Yield. The downstream evolution of mass flux (calculated using Eq. 3) of the reactants $\mathcal{A}$, the product $\mathcal{P}$ and $\mathcal{Q}$, and the yield $X_{\mathcal{Q}}$ is shown in Figure 11. Figure 11a confirms that reactant $\mathcal{A}$ can be considered as a conserved scalar for each Damköhler case; only a small fraction of the total mass flux injected is reacted away. In Figure 11b and 11c, it is shown that products $\mathcal{P}$ and $\mathcal{Q}$ are formed constantly. The ratio between the products, however, varies strongly with the Damköhler number, as illustrated by Figure 11d. For the low Damköhler case, the fraction of product $\mathcal{Q}$ formed is close to the kinematic limit of 0.001, whereas for the large Damköhler case the ratio is almost unity. Furthermore, it can be seen that the yield is almost uniform over the entire length of the reactor. Only close to the feed pipe, a small variation in the yield is found. This can be understood by considering the instantaneous velocity field shown in Figure 2; close to the feed pipe the jet and the wake enhance the turbulent fluctuations, whereas further downstream a more or less steady turbulent flow is formed.

For the low inlet concentration of $\mathcal{A}$, a significant relative decrease of the injected mass flux is found. Except for the lowest Damköhler number, in all cases the reactant has completely reacted away at the end of the reactor. Only in the lowest Damköhler case, about 70% is left. Note that it had already been found by the PDF shown in Figure 10g that this considerable mass-flux is formed by low concentrations of $\mathcal{A}$ only. For the low Damköhler number case, $\mathcal{A}$ is almost completely converted into $\mathcal{P}$ and hardly any $\mathcal{Q}$ is formed, resulting in a yield close to 0.001.

In Figure 12, the final yield is plotted against Damköhler number for both the low and the high concentration case. In both cases, it is again confirmed that limits of the mixing regions (kinematic and diffusion limited mixing) are correctly predicted. For Damköhler number around unity (where the turbulent and reaction time scales are about equal), also intermediate yields of $\mathcal{Q}$ are found. Most striking is the different behavior for the low and high inlet concentration case of reactant $\mathcal{A}$. For case H ($\phi_{\mathcal{A}0} = 4{,}000$), the transition from low to high $X_{\mathcal{Q}}$ is most gradual, extending over a range of almost seven orders of magnitude of Da, whereas in case L the yield increases from 10^{-3} to almost 1 over a range of about four order of magnitude of Da. Furthermore, in the low concentration case, product $\mathcal{Q}$ is formed at higher values for Da. In the previous paragraph, we observed that in case L, $\mathcal{A}$ becomes the

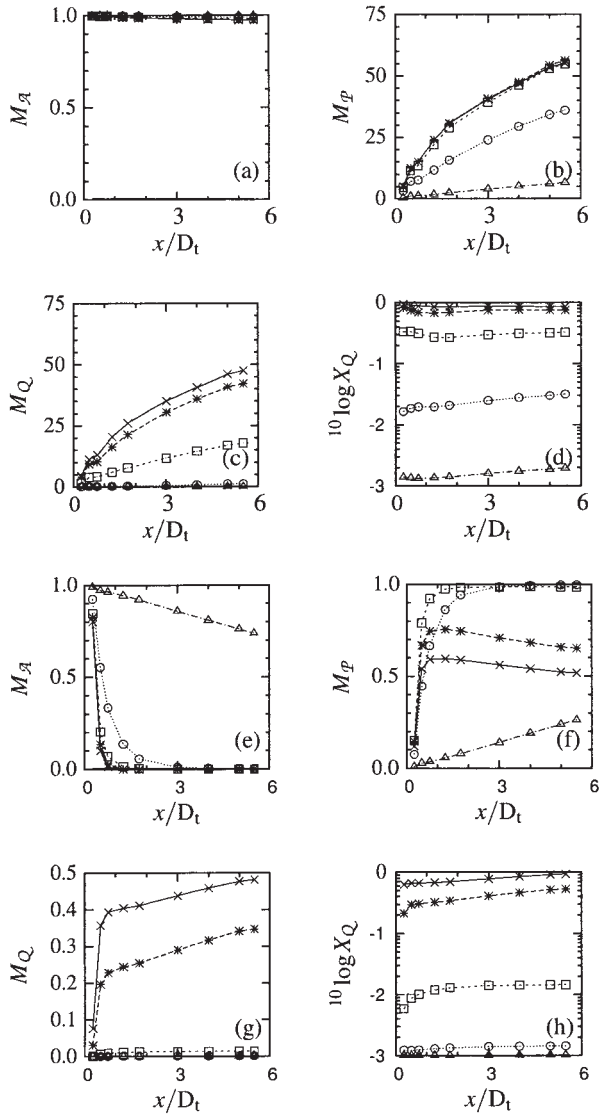

Figure 11. Downstream evolution of the total mass flux of reactant $\mathcal{A}$, the products $\mathcal{P}$ and $\mathcal{Q}$, and the yield $X_{\mathcal{Q}}$ for the high initial concentration of $\mathcal{A}$ (case H; fig. a–d) and the low initial concentration of $\mathcal{A}$ (case L; fig. e–h), shown for varying logarithm of the Damköhler number corresponding to cases defined in table 1: I = −4.3 (triangles); II = −2.3 (circles); III = −0.3 (squares); IV = 1.7 (asterisks); V = 3.7 (crosses).

limiting reactant. Although local shortages of $\mathcal{B}$ are formed, it was found that this also leads to a shortage of $\mathcal{A}$, and that, as a result, no product $\mathcal{Q}$ can be created.

Discussion and Conclusions

In this article, we have presented one of the first attempts to apply the FDF/LES methodology to a turbulent reactive flow in an industrial geometry. More in particular, the mixing of reacting scalars of a parallel competitive reaction scheme in a tubular reactor was investigated. Although FDF/LES is computationally very demanding (a parallel cluster of eleven dual processors has been kept busy for almost three months), this modeling approach is attractive because of the minimum of modeling assumptions required due to the ability to keep the reaction term closed. Closures have to be adopted for the nonresolved SGS scalar transport terms in the FDF equation (the SGS convective flux and the SGS dissipation), which were modeled by a gradient diffusion model (Eq. 12), and by the IEM model (Eq. 14), respectively.

The FDF closure models were assessed by means of experimental 2D-LIF data[22] of the mixing of a fluorescent dye in the flow of the TR operated at the same process conditions. The experimental 2D-LIF measurements of the scalar distribution over a horizontal and vertical cross-section showed that the global macro transport of the conserved scalar was qualitatively well predicted by the FDF numerical simulations; a nonuniform distribution of the scalar dye over the height of the reactor was found due to the upwardly inclined jet promoted by the blockage formed by the injector. Compared to the experimental results, however, the jet in the numerical simulation penetrates somewhat less deep into the reactor. Both the decay of the scalar mean and scalar variance along the center line of the reactor were overpredicted in the in the vicinity of the injector.

The findings above indicate that the FDF/LES simulation overpredict the mean spreading of the jet, and the dissipation of the small scale fluctuations in the vicinity of the injector. These effects were attributed to the overprediction of the turbulent diffusivity in the transition region (where the laminar jet meets the turbulent wake of the feedpipe). Since the eddy viscosity model employed in this research implicitly assumes fully developed turbulence, it does not capture the local suppression of small length scales in the laminar jet region. The resulting overprediction of the turbulent diffusivity leads to an overprediction of the FDF SGS scalar flux (causing the excessive spread of the mean). Also, it leads to an overprediction of the FDF dissipation due to an overestimation of the mixing frequency (causing the excessive decay of scalar variance). The problems are noticeable in the direct vicinity of the jet exit only, where the laminar jet emerges into the turbulent wake of the injector.

In spite of difficulties in jet region, it was shown that further downstream, the predicted scalar mean and variance closely agree with the experiments. Since the reactions mainly take

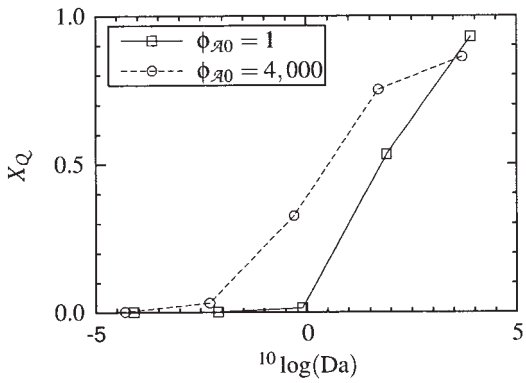

Figure 12. Final yield vs. Damköhler number for low and high inlet concentration of $\mathcal{A}$.

place in these regions, it is expected that the yield predictions are not too much affected. The qualitative behavior of the yield of the parallel competitive reactions indeed was well predicted, showing consistent physical behavior. The mixing limited and kinetic limited reaction were correctly predicted. The transition between the regimes occurred around $Da = 1.0$ for the low inlet concentration case, whereas in the high inlet concentration case the slow product $\mathcal{Q}$ is formed two orders of magnitudes earlier due to the excess of reactant $\mathcal{A}$. These observations may be important in process design in finding an optimal mixing intensity for given inlet concentration and flow conditions.

For more complicated fast reactions (such as fuel combustion or polymer reactions) it may be more important to correctly capture the scalar mixing in the vicinity of the jet. In order to take into account the local reduction of length scales, the use of dynamic subgrid scale models would be a better choice.[31,32] Furthermore, as long as the scalar spectrum has not fully developed (such as in the vicinity of the injector), it is not likely that a single turbulent Schmidt number is capable of correctly relating the turbulent diffusivity to the eddy viscosity as in Eq. 12. Particularly, for inhomogeneous turbulent flows in industrial process equipment, improved models have to be applied. A good candidate is the spectral relaxation (SR) model,[33] since it takes into account multiple time scales to explicitly incorporate the shape and development of the scalar spectrum by construction. An alternative model including multiple time scales is due to.[34]

In order to deal with the lack of intermittency and inability of the IEM model to modify the shape of the concentration PDF, several improved micro-mixing models are available. The "particle interaction model," the Langevin equation model and the Fokker-Planck closure can be used to establish stochastic mixing in the composition domain.[10,35] Drawbacks of the models, absence of relaxation to Gaussianity and unboundedness of the scalar fields, respectively, are prevented by a binomial sampling model[36] which combines the IEM and the particle interaction model.

In conclusion, the FDF/LES approach yields very detailed information on turbulent reactive flows with the usage of a minimum of modeling assumptions. In spite of the diverse and complex mechanisms of turbulence generation making the TR flow representative of industrial flows, a fair agreement for the conserved scalar mixing is obtained, with consistent physical behavior for the interaction of the chemical kinetics and the complex hydrodynamics. Although the high computational demands make FDF simulations currently accessible to academic research only, the exponential growth of computer resources will make them a versatile tool for process and geometry optimization of turbulent reactive flows in process industries. The primary focus should be on the development and incorporation of more sophisticated closure models into the FDF equation.

Notation

A = cross-section surface of the tubular reactor
$\mathbf{B}$ = scalar composition drift vector coefficient
$\mathbf{D}$ = drift vector coefficient
$D_t/D_f/D_i$ = diameter tubular reactor/feed pipe/injector hole
Da = Damköhler number
E = diffusion coefficient
$\mathbf{J} = J_i^{\alpha}$ = mass flux vector of specie α
M_j = streamwise mass flux of component j
N_s = number of species involved per reaction
N_p = number of Monte Carlo particles per grid cell
P_L = filtered density function
Re_i = Reynolds number based on jet
Re_f = Reynolds number based on feed pipe
Re_m = Reynolds number based on mean flow
$\mathbf{S}$ = resolved scale strain rate
$Sc_{(t)}$ = (Turbulent) Schmidt number
St = Strouhal number
U_m/U_f = mean velocity of main flow/jet
$\mathbf{W}$ = Wiener process vector
$X_{\mathcal{Q}}$ = yield of the slow product $\mathcal{Q}$
$\mathbf{f}$ = body force vector per unit of mass
k_1/k_2 = fast/slow reaction rate constant
p = pressure per unit of mass
$\mathbf{u}$ = velocity vector
$\mathbf{x}$ = position vector
$\mathcal{T}$ = turbulent macro time scale
$\mathcal{T}_{reaction}$ = characteristic reaction time
α = index scalar component vector
Γ/Γ_e = molecular/eddy diffusivity
δ = delta Dirac function
ρ = fine-grained density function
v/v_e = kinematic/eddy viscosity
σ_{α} = variance of scalar fluctuations of α
$\boldsymbol{\tau}_s$ = turbulent shear stress
$\boldsymbol{\phi}$ = composition vector
χ = scalar energy dissipation rate
$\boldsymbol{\psi}$ = value of composition vector
ω_{α} = reaction rate of component α
Ω_m = mixing frequency
DNS = direct numerical simulation
FDF = filtered density function
IEM = interaction by exchange with the mean
LES = large eddy simulation
LIF = laser induced fluorescence
MC = Monte Carlo
NS = Navier-Stokes
PDF = probability density function
SED = scalar energy dissipation
SGS = subgrid scale
SR = spectral relaxation
TR = tubular reactor

Literature Cited

1. Brethouwer, G., "Micro-Structure and Langrangian Statistics of the Scalar Field with a Mean Gradient in Isotropic Turbulence," *J. Fluid Mech.,* **474,** 193–255 (2003).
2. Bakker, R. A., and H. E. A. Van den Akker, "A Lagrangian Description of Micromixing in a Stirred Tank Reactor Using 1D-Micromixing Models in a CFD Flow Field," *Chem. Eng. Sci.,* **51**(11), 2643–2648 (1996).
3. Baldyga, J., and J. R. Bourne, "A Fluid Mechanical Approach to Turbulent Mixing and Chemical Reaction Part II Micromixing in the Light of Turbulence Theory," *Chem. Eng. Commun.,* **28,** 243–258 (1984).
4. McMurtry, P. A., T. C. Gansauge, A. R. Kerstein, and S. K. Krueger, "Linear Eddy Simulations of Mixing in a Homogeneous Turbulent Flow," *Phys. Fluids A,* **5**(4), 1023–1034 (1993).
5. Smagorinsky, J., "General Circulation Experiments with the Primitive Equations: 1. The Basic Experiment," *Mon. Weather Rev.,* **91,** 99 (1963).
6. Voke, P. R., "Subgrid-Scale Modelling at Low Mesh Reynolds Number," *Theoret. Comput. Fluid Dynamics,* **8,** 131–143 (1996).
7. Derksen, J. J., and H. E. A. Van den Akker, "Large Eddy Simulations on the Flow Driven by a Rushton Turbine," *AIChE J.,* **45**(2), 209–221 (1999).
8. Hollander, E. D., J. J. Derksen, and H. E. A. Van den Akker, "A Numerical Study on Othokinetic Agglomeration in Stirred Tanks," *AIChE J.,* **40**(11), 2425–2440 (2001).
9. Ten Cate, A., J. J. Derksen, H. J. M. Kramer, G. M. Van Rosmalen, and H. E. A. Van den Akker, "The Microscopic Modelling of Hydro-

dynamics in Industrial Crystallisers," *Chem. Eng. Sci.,* **56,** 2495–2509 (2001).
10. Pope, S. B., "Pdf Methods for Turbulent Reactive Flows," *Prog. Energy Combust. Sci.,* **11,** 119–192 (1985).
11. Steiner, H., and W. K. Bushe, "Large Eddy Simulation of a Turbulent Reacting Jet with Conditional Source-Term Estimation," *Phys. Fluids,* **13**(3), 754–769 (2001).
12. Wall, C., B. J. Boersema, and P. Moin, "An Evaluation of the Assumed Beta Probability Density Function Subgrid-Scale Model for Large Eddy Simulation of Nonpremixed, Turbulent Combustion with Heat Release," *Phys. Fluids,* **12**(10), 2522–2529 (2000).
13. Pope, S. B., "Computations of Turbulent Combustion: Progress and Challenges," *Proc. Combust. Inst.,* **23,** 591–612 (1990).
14. Gao, F., and E. E. O'Brien, "A Large Eddy-Simulation Scheme for Turbulent Reacting Flows," *Phys. Fluids A,* **5,** 1282 (1993).
15. Colucci, P. J., F. A. Jaberi, P. Givi, and S. B. Pope, "Filtered Density Function for Large Eddy Simulation of Turbulent Reacting Flows," *Phys. Fluids,* **10**(2), 499–515 (1998).
16. Zhou, X. Y., and J. C. F. Pereira, "Large Eddy Simulation (2D) of a Reacting Plane Mixing Layer Using Filtered Density Function Closure," *Flow, Turbulence and Combustion,* **64,** 279–300 (2000).
17. Jaberi, F. A., P. J. Colucci, S. James, P. Givi, and S. B. Pope, "Filtered Mass Density Function for Large-Eddy Simulation of Turbulent Reacting Flows," *J. Fluid Mech.,* **401,** 85–121 (1999).
18. Van Vliet, E., J. J. Derksen, and H. E. A. Van den Akker, "Modelling of Parallel Competitive Reactions in Isotropic Homogeneous Turbulence Using a Filtered Density Function Approach for Large Eddy Simulations," In *Proc. of the 3rd Int. Symp. on Comp. Techn. for Fluid/Thermal/Chemical Systems with Industrial Appl.,* Atlanta, GA (2001).
19. Cha, C. M., and P. Trouillet, "A Subgrid-Scale Mixing Model for Large-Eddy Simulation of Turbulent Reacting Flows Using the Filtered Density Function," *Phys. Fluids,* **15**(6), 1496–1504 (2003).
20. Gicquel, L. Y. M., P. Givi, F. A. Jaberi, and S. B. Pope, "Velocity Filtered Density Function for Large Eddy Simulation of Turbulent Flows," *Phys. Fluids,* **14**(3), 1196–1213 (2002).
21. Sheikhi, M. R. H., T. G. Drozda, P. Givi, and S. B. Pope, "Velocity-Scalar Filtered Density Function for Large Eddy Simulation of Turbulent Flows," *Phys. Fluids,* **15**(8), 2321–2337 (2003).
22. Van Vliet, E., S. M. Van Bergen, J. J. Derksen, L. M. Portela, and H. E. A. Van den Akker, "Time-Resolved, 3D, Laser-Induced Fluorescence Measurements of Fine-Structure Passive Scalar Mixing in a Tubular Reactor," *Exp. in Fluids,* **37,** 1–21 (2004).
23. Williamson, C. H. K., "The Existence of Two Stages in the Transition to Three-Dimensionality of a Cylinder Wake," *Phys. Fluids,* **31**(11), 3165–3137 (1988).
24. Deardorff, J. W., "A Numerical Study of Three-Dimensional Turbulent Channel Flow at Large Reynolds Numbers," *J. Fluid Mech.,* **41,** 453–480 (1970).
25. Zang, T. A., and U. Piomelli, *Large eddy simulation of transitional flow,* "Large Eddy Simulation of Complex Engineering and Geophysical Flows," B. Galperin and S. A. Orzag, eds., Cambridge University Press,p. (1993).
26. Van Driest, E. R., "On Turbulent Flow Near a Wall," *J. Aero. Sci.,* **23,** 1007–1011 (1956).
27. Frisch, U., B. Hasslacher, and Y. Pomeau, "Lattice-Gas Automata for the Navier-Stokes Equations," *Phys. Rev. Lett.,* **56**(14), 1505 (1986).
28. Somers, J. A., "Direct Simulation of Fluid Flow with Cellular Automata and the Lattice-Boltzmann Equation," *Appl. Sci. Res.,* **51,** 127–133 (1993).
29. O'Brien, E. E., "The Probability Density Function (pdf) Approach to Reacting Turbulent Flows," In: *Topics in Applied Physics: Turbulent Reacting Flows,* P. A. Libby and F. A. Williams, eds., **44**, 186–218 (1980).
30. Fox, R. O., *Computational Models for Turbulent Reacting Flows,* Cambridge University Press, (2003).
31. Pope, S. B., *Turbulent Flows,* Cambridge University Press, (2000).
32. Vreman, B., B. Geurts, and H. Kuerten, "Large-Eddy Simulation of Turbulent Mixing Layer," *J. Fluid Mech.,* **339,** 357 (1997).
33. Fox, R. O., "The Lagrangian Spectral Relaxation Model of the Scalar Dissipation in Homogeneous Turbulence," *Phys. Fluids,* **9**(8), (1997).
34. Heinz, S., and D. Roekaerts, "Reynolds Number Effects on Mixing and Reaction in a Turbulent Pipe Flow," *Chem. Eng. Science,* **56,** 3197–3210 (2001).
35. Fox, R. O., "The Focker-Planck Closure for Turbulent Molecular Mixing: Passive Scalars," *Phys. Fluids,* **4**(6), 1230–1244 (1992).
36. Valino, L., and C. Dopazo, "A Binomial Sampling Model for Scalar Turbulent Mixing," *Phys. Fluids A,* **2**(7), 1204–1212 (1990).

Manuscript received Aug. 26, 2003, and revision received July 9, 2004.